73rd International Astronautical Congress (IAC), Paris, France, 18-22 September 2022.

IAC-22-A6IP

Phase space description of the debris' cloud dynamics through a continuum approach

Giudici Lorenzo[a*], Trisolini Mirko[a], Colombo Camilla[a]

[a] *Department of Aerospace Science and Technology, Politecnico di Milano, Via La Masa 34, Milano 20156*, lorenzo1.giudici@polimi.it, trisolini.mirko@polimi.it, camilla.colombo@polimi.it
* Corresponding Author

Abstract

This paper proposes a continuity equation-based debris' evolutionary model for the long-term propagation of fragments' clouds under atmospheric drag, J_2 perturbation, solar radiation pressure and third-body perturbation. In particular, it focuses on enhancing the computational efficiency of the dynamical model. This purpose is achieved by cutting off some long-term effects of the perturbations, through averaging of the dynamics equations, and by deriving analytical expressions for the Earth's and Moon's ephemerides, through least squares fitting method. A new cost-free computation of the needed trace of the Jacobian for conservative forces is also proposed. The paper includes a validation phase, where the tool is applied to the modelling and propagation of two fragmentation clouds, characterised by a different dynamical regime, which allows to preliminarily identify some boundaries of applicability of the implemented dynamical model.
Keywords: Space debris, Orbital dynamics, Continuity equation

Nomenclature

L	=	Characteristic length, m
A/M	=	Area-to-mass ratio, m^2/kg
Δv	=	Ejection velocity, $\mathrm{m/s}$
λ	=	Logarithm to base 10 of L, m
χ	=	Logarithm to base 10 of A/M, m^2/kg
ν	=	Logarithm to base 10 of Δv, $\mathrm{m/s}$
p	=	Probability density function
P	=	Probability
$\boldsymbol{\alpha}$	=	Set of Keplerian elements (a, e, i)
$\boldsymbol{y}$	=	Variables $(a, e, i, \Omega, \omega, A/M)$

Acronyms/Abbreviations

MOC	=	Method Of Characteristics
SRP	=	Solar Radiation Pressure
TBP	=	Third-Body Perturbation
SBM	=	Standard Breakup Model
PDF	=	Probability Density Function
CDF	=	Cumulative Density Function
PDE	=	Partial Differential Equation
ODE	=	Ordinary Differential equation

1. Introduction

The number of services provided by in-orbit satellites is increasing massively and, accordingly, our exploitation of the space environment. In recent years, the space community has progressively given attention to the space debris problem: the growth of man-made objects can no longer be uncontrolled, to avoid the collapse of such a delicate ecosystem.

In this scenario, the development of tools to estimate the evolution of clouds of fragments is of paramount importance. On one hand, they allow the prediction of the trend of uncontrolled orbiting objects, naturally moving under the orbital perturbations. On the other, if combined with sustainability indices, they provide useful information to identify the most dangerous regions in case of a new fragmentation, helping to take go/no-go decisions for future missions.

Several methods have been developed to simulate the breakup of objects in space and the dynamical evolution of the generated clouds [1][2][3]. To address the propagation of huge population of fragments within a feasible computational time, recent studies have converged to the modelling of space debris no longer as single pieces but as a cloud, described in a probabilistic fashion and propagated according to the continuity equation [4][5][6][7]. Most of the developed density-based tools work in the low-Earth orbital region, where the Solar Radiation Pressure (SRP) and Third-Body Perturbation (TBP) can be neglected. Under this simplified dynamical regime, solutions to the continuity equations have been found either analytically [8] or via numerical integration [9][10][11].

This paper proposes a density-based model capable of propagating clouds of fragments, at a competitive computational cost, under the main orbital perturbations: atmospheric drag, J_2, SRP and TBP. This objective is achieved by filtering out the short-term and some long-

term oscillations of the orbital elements, through averaging of the dynamics equations. An efficient ephemerides model, based on the least squares fitting method, is implemented, allowing to retrieve the Moon's and Earth's slow-varying orbital elements in an efficient way. In addition, the structure of the Lagrange planetary equations is exploited to evaluate the divergence of the dynamics without computing any of the second partial derivatives of the disturbing potential, saving CPU time.

The paper is organised as follows:

- Section 2: description of the developed model for estimating the space debris' density distribution as consequence of a fragmentation event.
- Section 3: explanation of the propagation tool. The dynamical model implemented is here presented, with particular focus on the third-body perturbation model. A new equation for evaluating the needed divergence of conservative force fields is also proposed.
- Section 4: the developed debris' evolutionary model is applied to the modelling and propagation of a potential fragments' cloud on a Molniya orbit.
- Section 5: the main achievements of the paper are here recapped. The next steps to be addressed are also discussed.

2. Probabilistic cloud sampling through binning

This section is devoted to recap the model for the estimation of the debris density as a consequence of a fragmentation event, and the cloud sampling for the subsequent propagation, proposed in a past work and adopted in this paper. The idea, firstly proposed in [12] and then refined in [13], is to define, through probabilistic considerations, the domain in Keplerian elements and area-to-mass ratio that the fragments will occupy after a fragmentation event and to estimate the density in all regions belonging to it, through a binning approach. If the grid is fine enough, despite of the discontinuous nature of the method, the computed density distribution well represents the initial cloud of fragments.

2.1 Break up model

As commonly done in most of the probabilistic space debris models [8][11], the NASA Standard Breakup Model (SBM) [14] is adopted for characterising the ejected fragments in terms of characteristic length L, area-to-mass ratio A/M and ejection velocity magnitude Δv. Following the approach proposed in [11], the model is here reformulated from a probabilistic perspective, by modelling the fragments as a cloud described through three Probability Density Functions (PDF) in logarithm to base 10 of:

- Characteristic length λ, p_λ.
- Area-to-mass ratio χ, given λ, $p_{\chi|\lambda}$.
- Ejection velocity ν, given χ, $p_{\nu|\chi}$.

The expressions of $p_\lambda, p_{\chi|\lambda}$ and $p_{\nu|\chi}$ can be found in [11].

2.2 Reachable phase space domain

Boundaries in area-to-mass ratio A/M and ejection velocity Δv are firstly computed on the basis of the PDFs defined in Section 2.1, and then they are converted into the target domain in Keplerian elements, by introducing the ejection velocity angles and adopting the non-linear Cartesian-to-Keplerian coordinates transformation.

2.2.1 Boundaries in A/M and Δv

As remarked in [13], of the three variables upon which the PDFs of Section 2.1 depend, the distribution of the fragments in area-to-mass ratio χ and ejection velocity ν is sufficient to estimate the future evolution of the cloud under the orbital perturbations, according to the dynamical model adopted in this paper (Section 3). As a result, the PDFs can be marginalised over characteristic length L, without losing any needed information. As demonstrated in [13], if the domain in χ is split into N_χ bins, the 2D domain $\mathcal{D}_{\chi,\nu}$ hosting a fraction ζ of the total number of fragments can be bounded by 2 limit values in χ, χ_0 and χ_{N_χ}, and N_χ values in ν, ν_j. Indeed, note that the velocity distribution $p_{\nu|\chi}$ is conditional and, thus, it varies depending on the value of area-to-mass ratio. As a result, each area-to-mass ratio bin is characterised by a different limit in ejection velocity. The $N_\chi + 2$ limit values can be found by solving the following system of $N_\chi + 2$ non-linear equations [13]:

$$\begin{cases} \sum_{j=1}^{N_\chi} P_{\nu|\chi}(\bar{\chi}_j, \nu_j)\, P_\chi(\chi_{j-1} < \chi \leq \chi_j) = \zeta \\ p_{\nu|\chi}(\nu_1, \bar{\chi}_1)\bar{p}_\chi^{(1)} = p_{\nu|\chi}(\nu_2, \bar{\chi}_2)\bar{p}_\chi^{(2)} \\ \vdots \\ p_{\nu|\chi}\left(\nu_{N_\chi-1}, \bar{\chi}_{N_\chi-1}\right)\bar{p}_\chi^{(N_\chi-1)} = \cdots \\ p_{\nu|\chi}\left(\nu_{N_\chi}, \bar{\chi}_{N_\chi}\right)\bar{p}_\chi^{(N_\chi)} \\ P_\chi\left(\chi_0 < \chi \leq \chi_{N_\chi}\right) = \dfrac{\sqrt{1+8\zeta}}{2} - \dfrac{1}{2} \\ p_\chi(\chi_0) = p_\chi\left(\chi_{N_\chi}\right) \end{cases} \quad (1)$$

where P_χ and $P_{\nu|\chi}$ are the Cumulative Density Functions (CDF) of p_χ and $p_{\nu|\chi}$, χ_0 and χ_{N_χ} are the needed limit values in logarithm to base 10 of area-to-mass ratio, ν_j are the boundary values in logarithm to base 10 of ejection velocity, for each bin in χ, and the terms $\bar{\chi}_j$ are defined as:

$$\bar{\chi}_j = \frac{\chi_{j-1} + \chi_j}{2} \tag{2}$$

Note that the PDF in χ, p_χ, is occasionally replaced by $\bar{p}_\chi^{(j)}$ in Eq. (1), which represents the average value of p_χ over the j[th] bin in area-to-mass ratio, computed as:

$$\bar{p}_\chi^{(j)} = \frac{P_\chi\left(\chi_{j-1} < \chi \leq \chi_j\right)}{\delta\chi_j} \tag{3}$$

with $\delta\chi_j$ bin-size. Eq. (1) is solved combining a root finding algorithm and a non-linear programming algorithm, as detailed in [13].

2.2.2 Domain in Keplerian elements and A/M

As it will be shown in Section 3, the target phase space is a 6D phase space in the slow-varying Keplerian elements (i.e., semi-major axis a, eccentricity e, inclination i, right ascension of ascending nodes Ω, argument of periapsis ω), and area-to-mass ratio. Hence, the information on the spreading of the fragments in the 2D domain in χ, v, obtained by solving Eq. (1), must be converted into a domain in Keplerian elements and area-to-mass ratio.

Following the same approach adopted in [12], and reproposed in [13], the fragments are assumed to share the same initial position (i.e., the fragmentation location), which implies that only 3 out of the 6 Keplerian elements can freely vary, in order for the new orbit to intersect the parent orbit in the fragmentation point [11]. As a result, the needed domain is defined in a subset of 3 Keplerian elements $\boldsymbol{\alpha}$; semi-major axis a, eccentricity e and inclination i are here selected as independent variables. Nevertheless, the velocity magnitude with which the fragments are ejected from the parent object is not sufficient to determine the orbits on which they are injected, as the information on the direction of the impulse is missing. As commonly done in the literature [8][10], the ejection velocity is assumed to be isotropically distributed in direction, identified by the in-plane γ and out-of-plane φ angles. As demonstrated in [11], the isotropic distribution in direction translates into the following PDFs in γ, p_γ, and φ, p_φ:

$$\begin{aligned} p_\gamma &= \frac{1}{2\pi} \\ p_\varphi &= \frac{\cos\varphi}{2} \end{aligned} \tag{4}$$

The one-to-one correspondence that maps each limit in ejection velocity ($\Delta v_j = 10^{v_j}$) into a domain in Keplerian elements is obtained through:

- Averaging over the in-plane γ and out-of-plane φ ejection velocity angles.
- Maximisation over the ejection velocity magnitude Δv.

This ensures that the regions of the phase space with very little probability of hosting an ejected fragment are discarded.

The procedure to compute the domains in Keplerian elements $\mathcal{D}_{\boldsymbol{\alpha}}^{(j)}$ translates in the following set of equations:

$$\mathcal{D}_{\boldsymbol{\alpha}}^{(j)} = \left[\boldsymbol{\alpha}_P + f_s \cdot \overline{\Delta\boldsymbol{\alpha}^-}^{(j)}, \boldsymbol{\alpha}_P + f_s \cdot \overline{\Delta\boldsymbol{\alpha}^+}^{(j)}\right] \tag{5}$$

where $\boldsymbol{\alpha}_P$ identifies the parent object independent Keplerian elements, f_s is a safety factor, and $\overline{\Delta\boldsymbol{\alpha}^-}^{(j)}$, $\overline{\Delta\boldsymbol{\alpha}^+}^{(j)}$ are the maximum averaged negative and positive variations of the independent Keplerian elements for the j[th] bin, given Δv_j, computed as follows [13].

$$\begin{aligned} &\overline{\Delta\boldsymbol{\alpha}^\pm}_i^{(j)}\left(\Delta v_j\right) \\ &= \max_{\Delta v \leq \Delta v_j} \int_{\gamma_{1_i}^\pm}^{\gamma_{2_i}^\pm} \int_{\varphi_{1_i}^\pm}^{\varphi_{2_i}^\pm} \Delta\boldsymbol{\alpha}_i(\Delta v, \gamma, \varphi)\, p_\gamma p_\varphi \mathrm{d}\varphi\, \mathrm{d}\gamma \end{aligned} \tag{6}$$

where the plus and minus signs indicate the regions of the 2D domain $\mathcal{D}_{\gamma,\varphi}$ that lead to either positive or negative variations of the i[th] Keplerian element $\boldsymbol{\alpha}_i$. The non-linear relations that allow to compute the variation of the independent Keplerian elements $\Delta\boldsymbol{\alpha}_i$, given $\Delta v, \gamma, \varphi$, can be found in [12][13].

2.3 Domain discretisation

Once the domain in Keplerian elements and area-to-mass ratio is defined, the objective is to discretise it and compute a density value for each generated bin. As a result, the smaller is the variation of the density across a bin, the more accurate the discretised density distribution is, if compared to the actual one. Therefore, it is reasonable to ask for a step-size in the independent Keplerian elements $\boldsymbol{\delta\alpha}$ inversely proportional to the gradient of the density. Since the current model adopts an equally sized binning approach, the step-sizes are kept constant throughout the domain; hence, instead of the local gradient of the density, an average value is considered for setting the step-sizes, according to the following equation [13]:

$$\boldsymbol{\delta\alpha} = \left(\overline{\overline{\left|\nabla_{\boldsymbol{\alpha}}\, p_{v,\chi}\right|}}\right)^{-1} k \max_{\chi,v \in \mathcal{D}_{\chi,v}} p_{v,\chi} \tag{7}$$

The step-sizes computed according to Eq. (7) ensure that, on average, the variation in the PDF $p_{v,\chi}$ associated to a step $\boldsymbol{\delta\alpha}_i$ coincides with a fraction k of the maximum density value in the domain $\mathcal{D}_{\chi,v}$, which is taken as reference value.

2.4 Density estimation and sampling

The PDF in the subset of Keplerian elements $\boldsymbol{\alpha}$ and area-to-mass ratio A/M, $p_{\boldsymbol{x}}$, can be computed from $p_{v,\chi}$ through change of variables [10], as follows.

$$p_{\boldsymbol{x}} = \frac{p_{\nu,\chi}\left(\psi_{\boldsymbol{v}\to\boldsymbol{\alpha}}(\boldsymbol{\alpha})\right)}{|\det J_{\boldsymbol{v}\to\boldsymbol{\alpha}}|} \tag{8}$$

where $\psi_{\boldsymbol{v}\to\boldsymbol{\alpha}}$ is the transformation from the velocity vector $\boldsymbol{v} = \boldsymbol{v}_P + \Delta\boldsymbol{v}$ to the subset of Keplerian elements $\boldsymbol{\alpha}$, and $J_{\boldsymbol{v}\to\boldsymbol{\alpha}}$ is the Jacobian of the transformation, which can be found in [15].

The average value of the PDF of Eq. (8) in each bin of the reachable domain computed in Section 2.2 is computed through an "adaptive" Monte Carlo sampling, where the number of samples upon which the average is taken is varied according to the local value of the density gradient [13].

As it will be detailed in Section 3, the density distribution is propagated through the Method Of Characteristics (MOC) [16], which means that a population of samples must be extracted from the computed density distribution. The initial characteristics are uniformly sampled from the reachable domain $\mathcal{D}_{\boldsymbol{\alpha},A/M}$, simply extracting one sample from each bin.

3. Debris cloud propagation through the MOC

The density distribution is propagated numerically integrating the continuity equation, which is a Partial Differential Equation (PDE) that reads:

$$\frac{\partial n_{\boldsymbol{x}}}{\partial t} + \nabla_{\boldsymbol{y}} \cdot n_{\boldsymbol{x}}\boldsymbol{F} = 0 \tag{9}$$

where $\boldsymbol{F} = \frac{\mathrm{d}\boldsymbol{y}}{\mathrm{d}t}$ is the dynamics, and $n_{\boldsymbol{x}}$ is the phase space density, which is computed from the PDF of Eq. (8) through the following relation:

$$n_{\boldsymbol{x}} = N p_{\boldsymbol{x}} \tag{10}$$

with N total number of fragments generated by the fragmentation event. The MOC [16] allows transforming the PDE of Eq. (9) into an Ordinary Differential Equation (ODE), as follows.

$$\begin{cases} \dfrac{\mathrm{d}\boldsymbol{y}}{\mathrm{d}t} = \boldsymbol{F} \\ \dfrac{\mathrm{d}n_{\boldsymbol{x}}}{\mathrm{d}t} = -n_{\boldsymbol{x}}\,\nabla_{\boldsymbol{y}} \cdot \boldsymbol{F} \end{cases} \tag{11}$$

It is worth noticing that the variables $\boldsymbol{y}$ differ from the subset $\boldsymbol{x}$ upon which the density depends. They represent the least number of variables, whose dynamical evolution is either of interest or is needed for evaluating the force model $\boldsymbol{F}$. The most extended set of variables $\boldsymbol{y}$ considered in this paper is made up of the slow-varying orbital elements and area-to-mass ratio, as the dynamics equations are always averaged over the fast angular variable. Indeed, the debris evolutionary model developed in this work aims to estimate the long-term evolution of a potential cloud of fragments; to this purpose, cutting off the short-term oscillation in the orbital elements by averaging the dynamics over one orbital period allows to reduce the computational cost. The dependent orbital elements in $\boldsymbol{y}$ at fragmentation epoch are retrieved from the independent ones $\boldsymbol{\alpha}$, by imposing intersection with the parent orbit in the fragmentation point [13].

It is worth noticing that, to propagate the fragmentation cloud, not only the dynamics equations need to be evaluated, but also their divergence with respect to the variables $\boldsymbol{y}$, i.e., the trace of the Jacobian $\mathrm{tr}(J_{\boldsymbol{F}})$.

3.1 Dynamical model

In this section, the dynamical models considered in this work are presented. It is worth reminding that the main objective of the paper is to extend the debris evolutionary model to any orbital regime, obtaining sufficiently accurate results with a reasonable computational cost. The third-body perturbation demonstrated to be the most demanding in terms of CPU cost, as it typically requires a massive number of integration points to fulfil the imposed tolerances, whenever its effect becomes significant. The evaluation of the Moon and Sun ephemerides also contributes considerably to the cost. Therefore, this paper investigates different models for the third-body perturbation, both in terms of dynamics equations and ephemerides, while a single model of drag, Earth gravity field and solar radiation pressure is considered.

3.1.1 Drag model

The effect of drag is accounted through the superimposed King-Hele approximation proposed in [17]. It models the atmosphere as a sum of exponential functions:

$$\rho_s(h) = \sum_{p=1}^{n_p} \rho_p(h) = \sum_{p=1}^{n_\mathrm{p}} \hat{\rho}_p e^{-h/H_p} \tag{12}$$

where the number of the partial atmospheres, n_p, the partial reference densities, $\hat{\rho}_p$, and the partial scale heights, H_p, are obtained from a fit to a density model (Jacchia-77 in this work). The secular variation of semi-major axis a and eccentricity e is derived as a sum of King-Hele's expressions [18]. This allows to overcome the constraint enforced by the King-Hele model, which imposes the atmospheric density ρ to be strictly exponentially decaying with altitude h (i.e., a fixed scale height). Indeed, if the partial scale heights H_p are constant, the superimposed scale height H_s is not as such. It takes the following expression [17]:

$$H_p = -\frac{\rho_s(h)}{d\rho_s/dh} = \frac{\sum_{p=1}^{n_p} \rho_p(h)}{\sum_{p=1}^{n_p} \rho_p(h)/H_p} \tag{13}$$

Note that the superimposed atmosphere model can only be fitted to atmosphere models in altitude ranges where $\mathrm{d}H/\mathrm{d}h > 0$. The resulting dynamics equations are not here reported for brevity, but full details of the theory can be found in [17].

3.1.2 Earth gravity field model

In this paper, only the Earth's oblateness J_2 is added to the Keplerian term to describe the gravity field of the Earth. As well known in the literature, the J_2 perturbations causes secular variations only in right ascension of ascending nodes Ω and argument of perigee ω (and mean anomaly, here not considered), according to the following expressions:

$$\begin{aligned} \dot{\Omega} &= -W\frac{\cos i}{(1-e^2)^2} \\ \dot{\omega} &= W\frac{5\cos^2 i - 1}{2(1-e^2)^2} \end{aligned} \tag{14}$$

with W oblateness parameter defined as:

$$W = \frac{3}{2}J_2\frac{R_{\mathrm{Earth}}^2}{a^2}n \tag{15}$$

where R_{Earth} is the Earth's mean radius, and n mean motion.

3.1.3 Solar radiation pressure model

The effect of solar radiation pressure is included through a cannonball model, which approximates the acceleration induced by the impacting photons as:

$$a_{SRP} = p_{SRP}c_R A/M \tag{16}$$

where $p_{SRP} = 4.56 \times 10^{-6}\ \mathrm{N/m^2}$ is the solar pressure at 1 AU, c_R is the fragments' reflectivity coefficient, and A/M is the fragments' area-to-mass ratio. The model does not consider eclipses, which implies that SRP is assumed to be conservative [19], and, thus, its effect can be estimated integrating the Lagrange planetary equations. The disturbing potential due to SRP, R_{SRP}, takes the following expression [20]:

$$\begin{aligned} R_{SRP} = -\sigma n a^2 (x\cos\lambda_{\mathrm{Sun}} + \cdots \\ y\sin\lambda_{\mathrm{Sun}}\cos\varepsilon + z\sin\lambda_{\mathrm{Sun}}\sin\varepsilon) \end{aligned} \tag{17}$$

where $\sigma = \frac{a_{SRP}}{\mu}a^2$ is the ratio between the gravitational force and SRP force, λ_{Sun} is the longitude of the Sun measured in the Earth orbital plane, ε is the angle between the Earth orbital plane and the equator, and x, y, z are the fragments' coordinates in the Earth's centred equatorial reference frame. The longitude of the Sun λ_{Sun} and the obliquity of the ecliptic ε are computed analytically with the Meeus algorithm [21]. The fragments' coordinates can be written as function of the orbital elements, as follows.

$$\begin{aligned} x &= r(\cos\lambda\cos\Omega - \sin\lambda\sin\Omega\cos i) \\ y &= r(\cos\lambda\sin\Omega + \sin\lambda\cos\Omega\cos i) \\ z &= r\sin\lambda\sin i \end{aligned} \tag{18}$$

where $\lambda = \omega + f$ is the fragments' true latitude, and $r = \frac{a(1-e^2)}{1+e\cos f}$ is the fragments' orbital radius. The averaged disturbing potential can be found integrating Eq. (17) over mean anomaly, as follows.

$$\bar{R}_{SRP}(\boldsymbol{y}) = \frac{1}{2\pi}\int_0^{2\pi} R_{SRP}(\boldsymbol{y}, f)\frac{\mathrm{d}M}{\mathrm{d}f}\,\mathrm{d}f \tag{19}$$

with $\frac{\mathrm{d}M}{\mathrm{d}f} = \frac{(1-e^2)^{\frac{3}{2}}}{(1+e\cos f)^2}$. The expression of the averaged potential can be found in [20].

3.1.4 Third-body perturbation model

As already remarked at the beginning of Section 3.1, the TBP significantly impacts on the computational cost for the propagation of a population of characteristics. Indeed, whenever its effect cannot be neglected, the number of integration steps required by the numerical integrator increases substantially. As a result, not only the TBP model and the needed ephemerides has to be evaluated at a high rate, but also all the other perturbation models are computed redundantly, as they must adapt to the required integration step. Therefore, besides the single averaged formulation of the third-body disturbing potential $\bar{R}_{3B}$, this paper investigates the possibility of adopting the double $\bar{\bar{R}}_{3B}$ averaged formulation; this second option adds a second integration over the third body mean anomaly, cutting off the associated long-term oscillations. The slower dynamics is expected to relax the constraint on the integration step, but it must be analysed whether the simplified dynamics preserves a sufficiently high accuracy for the purpose of the method, at least in a well-defined region of the phase space.

The third-body disturbing potential R_{3B} is written as a series expansion in the parallactic ratio $\delta = a/r_{3B}$, as follows [22][23].

$$R_{3B} = \frac{\mu_{3B}}{r_{3B}}\sum_{k=2}^{\infty}\delta^k\left(\frac{r}{a}\right)^k P_k(\cos\phi) \tag{20}$$

where $\mu_{3\mathrm{B}}$ is the third body gravitational parameter, r_{3B} is the third body distance from the central planet, and ϕ is the angle between the fragments and the third body position vector measured from the central planet, i.e.:

$$\cos\phi = \frac{\boldsymbol{r}\cdot\boldsymbol{r}_{3B}}{r\,r_{3B}} = \hat{\boldsymbol{r}}\cdot\hat{\boldsymbol{r}}_{3B} \tag{21}$$

The direction $\hat{\boldsymbol{r}}$ can be written as function of the fragments' orbital elements through the following relation:

$$\hat{\boldsymbol{r}} = \hat{\boldsymbol{P}} \cos f + \hat{\boldsymbol{Q}} \sin f \tag{22}$$

where $\hat{\boldsymbol{P}}$ and $\hat{\boldsymbol{Q}}$ are the unit vectors in the direction of the eccentricity vector and semi-latus rectum, respectively. Eq. (22) allows the isolation of the terms dependent on true anomaly f, making the integration over mean anomaly of the disturbing potential easier. In this work, only the second order term of the series in Eq. (20) will be considered, which guarantees a sufficient level of accuracy when far enough from the disturbing body.

Single averaged formulation

The averaged disturbing function takes the following expression:

$$\begin{aligned}&\bar{R}_{3B}(a, e, i, \Omega, \omega, \boldsymbol{r}_{3B}) \\ &= \frac{1}{4}\frac{\mu_{3\mathrm{B}}}{r_{3B}}\delta^2(3A_{3B}^2(4e^2+1) + \cdots \\ &\quad 3B_{3B}^2(1-e^2) - 3e^2 - 2)\end{aligned} \tag{23}$$

with A_{3B} and B_{3B} defined as [24]:

$$\begin{aligned}A_{3B} &= \hat{\boldsymbol{P}} \cdot \hat{\boldsymbol{r}}_{3B} \\ B_{3B} &= \hat{\boldsymbol{Q}} \cdot \hat{\boldsymbol{r}}_{3B}\end{aligned} \tag{24}$$

As it can be noticed, the single averaged disturbing potential depends only on the third body position vector. Several analytical expressions for the position vector of the main celestial bodies have been derived, which can be found in the literature. This work adopts the Meeus algorithm to retrieve the position vector of the Moon and the Sun in the Earth's centred equatorial reference frame [21].

Double averaged formulation

The dependency of the third body position vector on the true anomaly is highlighted according to Eq. (22), substituting the terms $\hat{\boldsymbol{P}}, \hat{\boldsymbol{Q}}$ and f with $\hat{\boldsymbol{P}}_{3B}, \hat{\boldsymbol{Q}}_{3B}$ and f_{3B}. Hence, the terms A_{3B} and B_{3B} modifies as:

$$\begin{aligned}A_{3B} &= c_{11}\cos f_{3B} + c_{12}\sin f_{3B} \\ B_{3B} &= c_{21}\cos f_{3B} + c_{22}\sin f_{3B}\end{aligned} \tag{25}$$

with $c_{11} = \hat{\boldsymbol{P}} \cdot \hat{\boldsymbol{P}}_{3B}$, $c_{12} = \hat{\boldsymbol{P}} \cdot \hat{\boldsymbol{Q}}_{3B}$, $c_{21} = \hat{\boldsymbol{Q}} \cdot \hat{\boldsymbol{P}}_{3B}$ and $c_{22} = \hat{\boldsymbol{Q}} \cdot \hat{\boldsymbol{Q}}_{3B}$. The double averaged expression of the disturbing potential can be obtained averaging Eq. (23) over third body mean anomaly M_{3B}, which leads to the following expression.

$$\begin{aligned}&\bar{\bar{R}}_{3B}(a, e, i, \Omega, \omega, a_{3B}, e_{3B}, i_{3B}, \Omega_{3B}, \omega_{3B}) \\ &= \frac{\mu_{3B}}{8}\frac{a^2}{a_{3B}^3(1-e_{3B}^2)^{\frac{3}{2}}}(-2(2+3e^2) + \cdots \\ &\quad 3(4e^2+1)(c_{11}^2 + c_{12}^2) + \cdots \\ &\quad 3(1-e^2)(c_{21}^2 + c_{22}^2))\end{aligned} \tag{26}$$

Note that the dependency on the third body orbital elements is embedded in the c_{ij} terms. The drawback of the double averaged formulation is that the integration of the disturbing potential over the third body mean anomaly highlights the dependency on the other five Keplerian elements. Therefore, the information of the third body position vector is no longer sufficient. Retrieving the Luni-Solar ephemerides from online libraries, as the SPICE/MICE NASA toolkit, would nullify the advantage of the double averaged formulation in terms of computational costs. Therefore, this work derives analytical expressions, valid over a defined time window, for all the Moon's and Earth's slow-varying Keplerian elements through least squares interpolation. The fitting function adopted merges a Fourier series with a polynomial term, as follows.

$$\begin{aligned}\beta_i = \sum_{k=1}^{N_f}[&A_k \cos\big(k\pi(2\tilde{t}-1)\big) + \cdots \\ &B_k \sin\big(k\pi(2\tilde{t}-1)\big)] + \sum_{k=0}^{N_p} C_k \tilde{t}^k\end{aligned} \tag{27}$$

with $\tilde{t} \in [0, 1]$ adimensional time, that avoids the polynomial coefficients of the higher order terms to become too small, complicating the convergence of the least squares method. Note that this is the most general function used; however, except for the right ascension of ascending nodes Ω_M and argument of periapsis ω_M of the Moon, the polynomial part is sufficient to capture the long-term evolution of the Earth's and Moon's Keplerian elements with respect to the equator. For the applications presented in Section 4, the Fourier expansion was carried out up to the 5th order, when needed, while the polynomial term up to the 3rd power, considering a 50 years' time-window, starting from 1st January 2000. In Figure 1 the resulting profiles of the Keplerian elements are compared to the actual ones, retrieved through the SPICE/MICE NASA toolkit. As it can be noted, the long-term behaviour is captured by the analytical model, while the short-term oscillations are filtered out. As a result, the semi-major axis and eccentricity of both Earth and Moon remain constant over time.

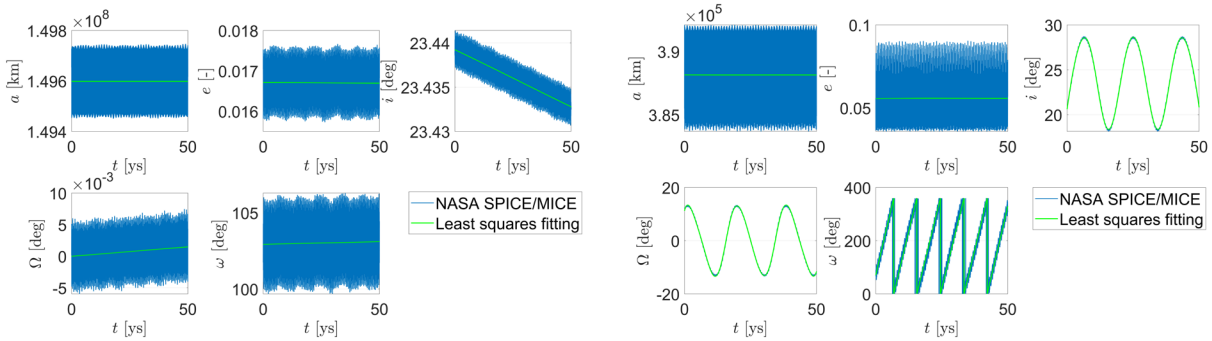

(a) Earth's Keplerian elements (b) Moon's Keplerian elements

Figure 1. Comparison between interpolated and SPICE/MICE slow-varying Keplerian elements.

3.2 Trace of the Jacobian for conservative forces

In principle, computing the divergence of the Lagrange planetary equations would mean evaluating several second partial derivatives of the disturbing potential with respect to the orbital elements. However, the structure of the dynamics equations can be beneficially exploited to ease the computation. Indeed, the Lagrange planetary equations [25] can be written in the following form:

$$\begin{aligned}
\frac{\mathrm{d}a}{\mathrm{d}t} &= C_{aM}(a)\frac{\partial R}{\partial M} \\
\frac{\mathrm{d}e}{\mathrm{d}t} &= C_{e\omega}(a,e)\frac{\partial R}{\partial \omega} + C_{eM}(a,e)\frac{\partial R}{\partial M} \\
\frac{\mathrm{d}i}{\mathrm{d}t} &= C_{i\Omega}(a,e,i)\frac{\partial R}{\partial \Omega} + C_{i\omega}(a,e,i)\frac{\partial R}{\partial \omega} \\
\frac{\mathrm{d}\Omega}{\mathrm{d}t} &= C_{\Omega i}(a,e,i)\frac{\partial R}{\partial i} \\
\frac{\mathrm{d}\omega}{\mathrm{d}t} &= C_{\omega e}(a,e)\frac{\partial R}{\partial e} + C_{\omega i}(a,e,\mathrm{i})\frac{\partial R}{\partial i} \\
\frac{\mathrm{d}M}{\mathrm{d}t} &= C_{Ma}(a,e)\frac{\partial R}{\partial a} + C_{Me}(a,e)\frac{\partial R}{\partial e}
\end{aligned} \tag{28}$$

with the C_{ij} terms having the following property:

$$C_{ij} = -C_{ji} \tag{29}$$

Therefore, since each C_{ij} term has a correspondent inverse C_{ji}, all the second partial derivatives of the disturbing potential R cancel out. By looking at the dependencies of the C_{ij} terms on the orbital elements, it can be inferred that the trace of the Jacobian reads:

$$\begin{aligned}
\mathrm{tr}(J_F) = &\frac{\partial C_{i\Omega}}{\partial i}\frac{\partial R}{\partial \Omega} + \cdots \\
&\left(\frac{\partial C_{e\omega}}{\partial e} + \frac{\partial C_{i\omega}}{\partial i}\right)\frac{\partial R}{\partial \omega} + \cdots \\
&\left(\frac{\partial C_{aM}}{\partial a} + \frac{\partial C_{eM}}{\partial e}\right)\frac{\partial R}{\partial M}
\end{aligned} \tag{30}$$

Note that, in case of averaged dynamics over mean anomaly M, the last term of Eq. (30) nullifies. The resulting trace of the Jacobian takes the following form:

$$\begin{aligned}
\mathrm{tr}(J_F) = \frac{1}{na^2e^2\sqrt{1-e^2}\sin^2 i}\Bigg(&e^2\cos i\frac{\partial \bar{R}}{\partial \omega} \\
&+ (\sin^2 i - e^2)\frac{\partial \bar{R}}{\partial \Omega}\Bigg)
\end{aligned} \tag{31}$$

It can be immediately understood that evaluating Eq. (31) instead of computing the partial derivatives of the dynamics equations for each orbital elements allows to reduce considerably the computational cost. In addition, by looking at Eq. (31), it can be noted that whenever the averaged disturbing potential does not depend on Ω and ω, the trace of the Jacobian is null. This is the case of the J_2 perturbation.

4. Case study

This section is devoted to the testing of the model presented in this paper. In particular, the analysis is focused on the comparison between the single and double averaged formulation of the third-body disturbing potential presented in Section 3.1.4.

4.1 Simulation setup

The method is applied to the potential fragmentation of payloads orbiting on Molniya orbits, a kind of orbit strongly influenced by the Luni-Solar perturbation. Two parent orbits are here considered, characterised by a different value of eccentricity; instead, the other orbital elements are kept fixed. The parent orbit's Keplerian elements are reported in Table 1.

Table 1. Parent orbit Keplerian elements.

a [km]	e [−]	i [°]	Ω [°]	ω [°]	f [°]
26600	0.5, 0.67	70	30	60	120

The choice of the eccentricity values was driven by two reasons: firstly, the lower eccentricity value guarantees that the effect of atmospheric drag is almost negligible for every generated fragment; on the other hand, the higher one is such that the parent perigee altitude reaches 400 km, at which the drag perturbation becomes predominant with respect to the other disturbing forces. Secondly, the two regions are populated by a high

number of satellites either of military or navigation type, and, thus, are potential hazardous orbits in case of fragmentation. In this eventuality, because of the low perigee altitude, the effect of such a cloud of fragments would be dangerous also for the vast population of satellites in low-Earth orbit. The values of right ascension of ascending nodes Ω, argument of perigee ω and true anomaly f are arbitrarily set.

Because of the low flux of debris in the Molniya orbital region, the application here presented considers the potential explosion of the satellites, rather than an in-orbit collision. The generated fragmentation cloud is propagated for 15 years under atmospheric drag, J_2 perturbation, SRP and TBP.

4.2 Results

Some relevant results of the simulation scenario explained at the beginning of the section are here presented. Firstly, the evolution of the debris' cloud, computed with the single averaged approach, is shown in terms of heatmaps in the five slow-varying orbital elements, to observe how the perturbations influence the cloud dynamics. Secondly, the single and double averaged formulations are compared, by plotting, at different epochs, the cumulative spatial density distributions.

4.2.1 Low-eccentricity case

In Figure 2 the density distributions at fragmentation epoch and 5, 10, and 15 years after the event are shown. As it can be noticed, the fragments, that are confined in a small region in Ω, ω at fragmentation, quickly spread out in the two variables under the effect of the J_2 perturbation. The effect of atmospheric drag is almost negligible for 10 years, as no circularisation of the orbit of any fragment is observed. However, in the last snapshot, a kind of tail appears in the a, e phase space, which is caused by the circularisation of the orbit of the fragments with the lowest radius of the perigee. This phenomenon happens only when the SRP and TBP increase the eccentricity value of such fragments, lowering their perigee altitude. The TBP effects may also be observed in the huge variations in inclination, as high as 10 degrees.

In Figure 3 the cumulative spatial density distributions 5, 10 and 15 years after fragmentation are plotted, superimposing the profiles deriving from the propagation with single and double averaged formulation of the third-body potential (blue and red solid lines), respectively. As expected, the number of in-orbit fragments barely changes over time. As it can be noted, the double average formulation accurately follows the reference profile in every snapshot. The figures also displays the percentage relative error $\mathrm{Err}_{\%}$ (green dashed line) between the two profiles, measuring the quality of the double averaged formulation against the single averaged one. It is computed as:

$$\mathrm{Err}_{\%}(\bar{x}) = \frac{|N_{SA}(x \leq \bar{x}) - N_{DA}(x \leq \bar{x})|}{N_{SA}^{\mathrm{tot}}} \qquad (32)$$

with x one of the variables among altitude h, longitude λ and latitude ϕ, and N_{SA}, N_{DA} the number of fragments estimated by the single and double averaged formations, respectively. The error keeps lower than 1% in all the considered snapshots and, more importantly, it just slightly increases over time. On the contrary, the two approaches shows a massive difference in terms of CPU cost, which is summarised in Table 2.

Table 2. Computational time for the 15 years' propagation of the debris cloud (10000 characteristics) with single and double averaged formulations of the third-body potential - Low eccentricity case (4 Intel(R) Xeon(R) CPUs E5-4620 v4 @ 2.10GHz, 10 physical/20 logical cores per CPU).

Single average	Double average
4876 s	299 s

The computational cost is lowered by a factor 16.3 by the double average approach.

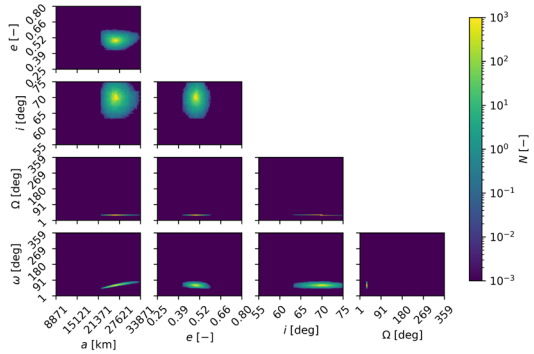

(a) 0 years after fragmentation.

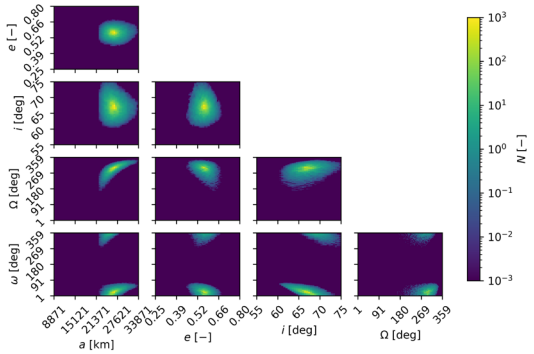

(b) 5 years after fragmentation.

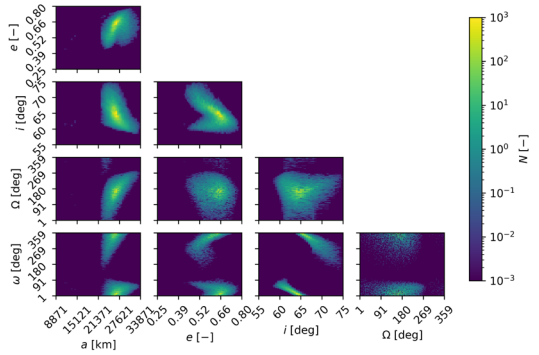

(c) 10 years after fragmentation.

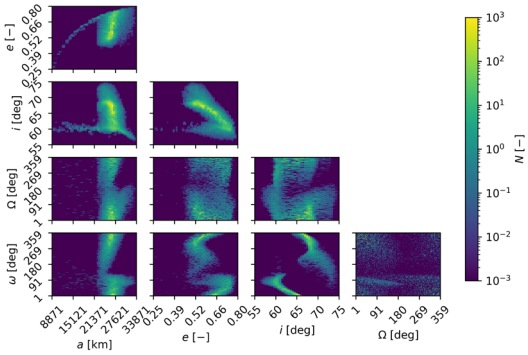

(d) 15 years after fragmentation.

Figure 2. Density distribution in the slow-varying orbital elements over time - Low eccentricity case.

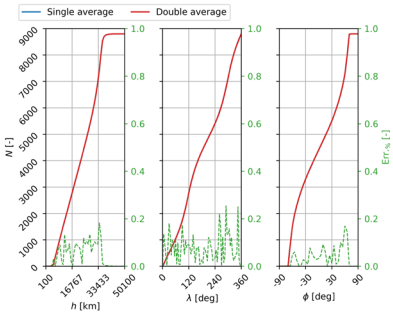

(a) 5 years after fragmentation.

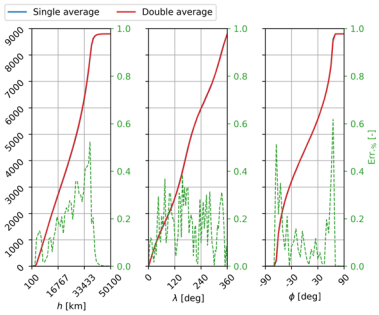

(b) 10 years after fragmentation.

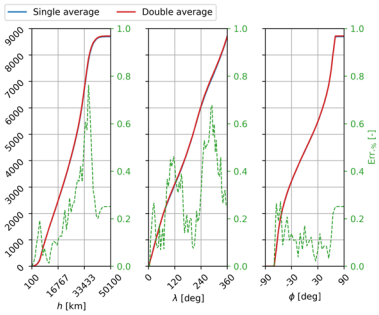

(c) 15 years after fragmentation.

Figure 3. Comparison in terms of spatial density distribution between single and double averaged third-body disturbing potential - Low eccentricity case.

4.2.2 High-eccentricity case

Figure 4 shows the density distributions for the high-eccentricity case. With respect to the low-eccentricity case, the cloud is hugely influenced by atmospheric drag, because the higher eccentricity value causes part of the distribution to cross a relatively high-density region of the atmosphere, even at fragmentation epoch. As a result, the circularisation of the orbit of such fragments takes place immediately. As it can be further observed, the debris cloud, which is continuous and smooth for the low-eccentricity case for the whole simulation time, here appears to be formed from scattered points. This effect is caused by the lower number of characteristics from which the density is retrieved, as part of them crosses the lowest part of the atmosphere (below 100 km) as time elapses, and thus is discarded.

As done in Section 4.2.1, In Figure 5 the cumulative spatial density distributions 5, 10 and 15 years after fragmentation are shown. In this second case, the number of fragments is almost halved at the end of the simulation. As it can be immediately inferred, the accuracy of the double averaged formulation is rougher; nevertheless, the relative error (green dashed line), which steadily increases over time, remains quite small and reaches the 8% at the final time considered. The double averaged formulation was 16.8 times faster in this second application.

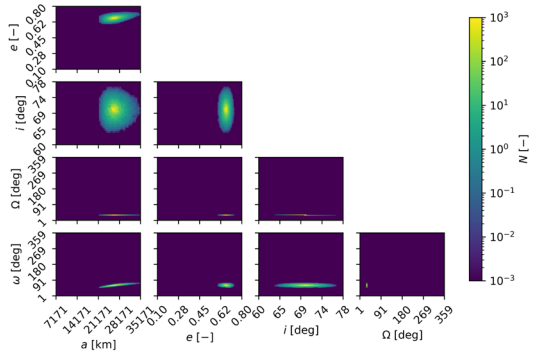

(a) 0 years after fragmentation.

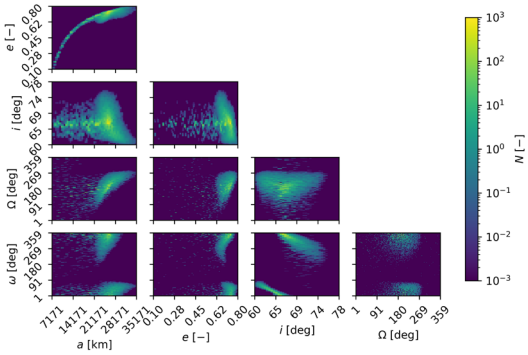

(b) 5 years after fragmentation.

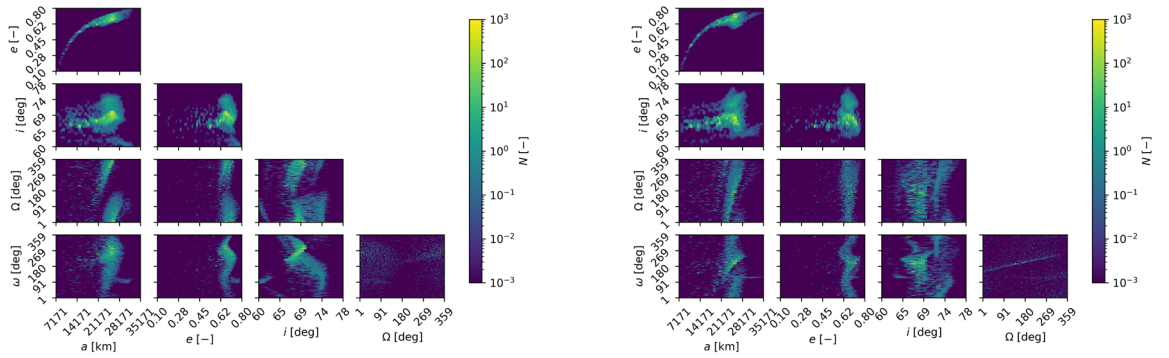

(c) 10 years after fragmentation. (d) 15 years after fragmentation.

Figure 4. Density distribution in the slow-varying orbital elements over time - High eccentricity case.

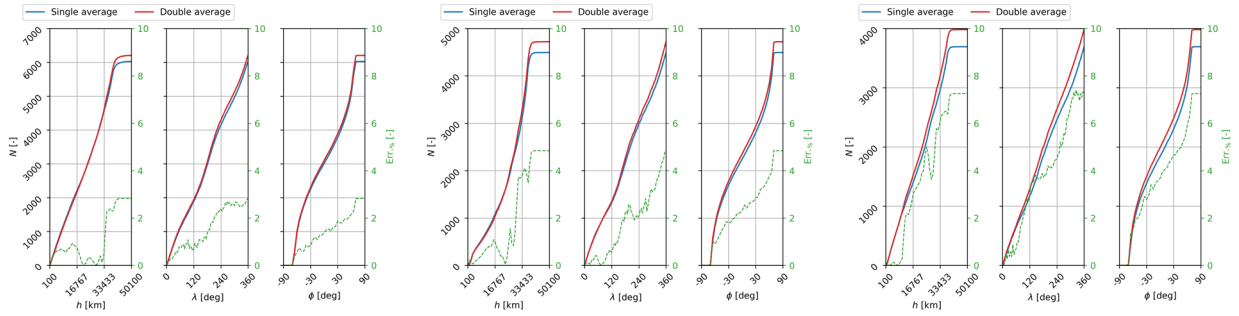

(a) 5 years after fragmentation (b) 10 years after fragmentation. (c) 15 years after fragmentation.

Figure 5. Comparison in terms of spatial density distribution between single and double averaged third-body disturbing potential - High eccentricity case.

The reason of this different behaviour can be understood propagating the parent orbit Keplerian elements reported in Table 1 with the single and double average approaches and comparing the resulting profiles. In Figure 6 the evolution of the perigee altitudes h_p for the two eccentricity values are shown. As it can be observed, for both the cases, the double averaged formulation tends to overestimate the perigee altitude over time. For the low-eccentricity case, this translates into a relative percentage error of roughly 1% at the end of the simulation. On the contrary, for the high-eccentricity case the difference between the two profiles is dramatic; in fact, in this second scenario, the propagated characteristic reaches an altitude of $250 - 300$ km after 5 years, where the atmospheric density increases rapidly while getting closer to Earth surface (i.e., the gradient of the atmospheric density is relatively high). As a result, the difference in altitude resulting from the two dynamical models causes the two profiles to come apart. For the single averaged formulation, the atmospheric drag predominates over the TBP, and the characteristic re-enters the atmosphere; on the other hand, for the double averaged formulation, the long-term periodic oscillation induced by the TBP continues, exceeding in magnitude the drag perturbation.

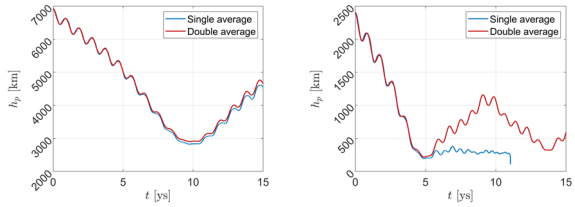

(a) Low-eccentricity case (b) High-eccentricity case

Figure 6. Perigee altitude profile for the low- and high-eccentricity cases - Comparison between single and double averaged third-body potential's formulations.

5. Conclusions

This paper proposed a density-based model for propagating clouds of debris under the main orbital perturbations: atmospheric drag, J_2, solar radiation pressure and third-body perturbation. This objective was already successfully achieved with a previous work, but this study aimed to considerably improve the computational efficiency of the method. Particular effort was devoted to the third-body perturbation model, which demonstrated to be the bottleneck in terms of CPU cost.

Three main aspects were here implemented and tested. Firstly, the double averaged formulation of the third-body disturbing potential was derived, integrating over

the third body mean anomaly. Secondly, analytical expressions for the long-term variation of Earth's and Moon's slow-varying orbital elements were obtained through least squares fitting method; the interpolating function adopted combined a polynomial term up to the third order and a Fourier series up to the fifth order, which guaranteed to replicate the celestial bodies' ephemerides for a 50-years' time-window. Finally, this work demonstrated the possibility of evaluating the trace of the Jacobian of non-conservative force models without computing any of the second partial derivatives of the disturbing potential, just exploiting the structure of the Lagrange planetary equations.

The simplified dynamical model was tested in the modelling and propagation of two potential clouds of fragments, generated by the explosion of a satellite orbiting on Molniya orbits, characterised by two different values of eccentricity. The accuracy of the model was verified against the single averaged approach, by comparing the cumulative clouds' spatial density distributions, at different time epochs. For the low-eccentricity case, the ejected fragments were barely affected by atmospheric drag, and the double averaged formulation demonstrated to be very accurate, with a relative error smaller than 1%. On the contrary, atmospheric drag was the dominant perturbation in the high-eccentricity case, causing a vast part of the cloud to re-enter the atmosphere. In this second scenario, the small error introduced by the double averaged formulation causes the fragments to face a very different atmosphere density, which translates into a considerable difference in trajectory. Nevertheless, the relative error remained modest over the time-window considered, although steadily increasing over time. In terms of computational cost, the double averaged formulation demonstrated to be more than 16 times faster.

Considering the competitiveness of the method in terms of computational cost and its high accuracy under certain dynamical conditions, future works will be dedicated to an extensive validation of the model to clearly define its boundaries of applicability, depending on the target level of accuracy.

Acknowledgements

This project has received funding from the European Research Council (ERC) under the European Union's Horizon 2020 research and innovation programme (grant agreement No 679086 - COMPASS) and from the European Space Agency contract 4000133981/21/D/KS.

References

[1] Rossi A., Lewis H., White A., Anselmo L, Pardini C., Krag H., Bastida Virgili B., Analysis of the consequences of fragmentations in low and geostationary orbits, Advances in Space Research, 57 (2016) 1652-1663.

[2] Liou J. C., Hall D. T., Krisko P. H., Opiela J. N., Legend – a three-dimensional LEO-to-GEO debris evolutionary model, Advances in Space Research, 34 (2004) 981-986.

[3] Lewis H. G., Swinerd G., Williams N., Gittins G., DEMAGE: a dedicated GEO debris model framework, 3rd European Conference on Space Debris, ESA/ESOC Darmstadt, Germany, 2001.

[4] Smirnov N. N., Dushin V. R., Panfilov I. I., Space debris evolution mathematical modelling, 1st European Conference on Space Debris, 1993.

[5] Nazarenko A. I., The development of the statistical theory of a satellite ensemble motion and its application to space debris modeling, 2nd European Conference on Space Debris, 1997.

[6] McInnes C. R., An analytic model for the catastrophic production of orbital debris, ESA Journal 17 (1993) 293-305.

[7] Letizia F., Colombo C., Lewis H., Analytical model for the propagation of small-debris-object clouds after fragmentations, Journal of Guidance, Control, and Dynamics 38 (2015) 1478-1491.

[8] Letizia F., Colombo C., Lewis H., Multidimensional extension of the continuity equation method for debris clouds evolution, Advances in Space Research 57 (2015) 1624-1640.

[9] Letizia F., Extension of the density approach for debris cloud propagation, Journal of Guidance, Control, and Dynamics, 41 (2018) 2651-2657.

[10] Frey S., Colombo C., Lemmens S., Application of density-based propagation to fragments cloud using the Starling suite, 1st International Orbital Debris Conference, Sugar Land, Texas, 2019, December 9-12.

[11] Frey S., Colombo C., Transformation of satellite breakup distribution for probabilistic orbital collision hazard analysis, Journal of Guidance, Control, and Dynamics, 44 (2021) 88-105.

[12] Giudici L., Colombo C., Trisolini M., Gonzalo J. L., Letizia F., Frey S., Space debris cloud propagation through phase space domain binning, Aerospace Europe Conference, Warsaw, Poland, 2021, November 23-26.

[13] Giudici L., Trisolini M., Colombo C., Probabilistic multi-dimensional debris cloud propagation subject to non-linear dynamics, Advances in Space Research, (2022) - submitted.

[14] Johnson N. L., Krisko P., Liou J. C., Nasa's new breakup model of evolve 4.0, Advances in Space Research, 28 (2001) 1377-1384.

[15] Gonzalo J. L., Colombo C., Di Lizia P., Analytical framework for space debris collision avoidance maneuver design, Journal of Guidance, Control and Dynamics, 44 (2021) 469-487.

[16] Jhon F., LaSalle J. P., Liou J. C., Partial Differential Equations, fourth ed., Springer, New York, 1991.
[17] Frey S., Colombo C., Lemmens S., Extension of the King-Hele orbit contraction method for accurate semi-analytical propagation of non-circular orbits, Advances in Space Research, 64 (2019) 1-17.
[18] King-Hele D., Theory of Satellite Orbits in An Atmosphere, Butterworhts Mathematical Text, London, 1964.
[19] Krivov V.A., Getino J., Orbital evolution of high-altitude balloon satellites, Atron. Astrophys., 318 (1997) 208-314.
[20] Gkolias I., Alessi E. M., Colombo C., Dynamical taxonomy of the coupled solar radiation pressure and oblateness problem and analytical deorbiting configuration, Celestial Mechanics and Dynamical Astronomy, 132 (2020) 55.
[21] Meeus J., Astronomical algorithms, Willmann-Bell, second ed., 1998.
[22] Kaufman B., Higher order theory for long-term behaviour of Earth and Lunar orbiters, National Technical Information Service, 1972.
[23] Colombo C., Long-Term Evolution of Highly Elliptical Orbits: Luni-Solar Perturbation Effects for Stability and Re-entry, Front. Astron. Space Sci., 2019.
[24] Blitzer L., Handbook of Orbital Perturbations, Tucson, AZ: University of Arizona, 1970.
[25] Vallado D. A., McClain W. D., Fundamentals of astrodynamics and applications, McGraw-Hill, 1997.